

MULTISCALE FLOW FOR ROBUST AND OPTIMAL COSMOLOGICAL ANALYSIS

PREPRINT, COMPILED JUNE 9, 2023

Biwei Dai^{a,b*} and Uroš Seljak^{a,b}

^aBerkeley Center for Cosmological Physics and Department of Physics, University of California, Berkeley, CA 94720, USA

^bLawrence Berkeley National Lab, 1 Cyclotron Road, Berkeley, CA 94720, USA

ABSTRACT

We propose Multiscale Flow, a generative Normalizing Flow that creates samples and models the field-level likelihood of two-dimensional cosmological data such as weak lensing. Multiscale Flow uses hierarchical decomposition of cosmological fields via a wavelet basis, and then models different wavelet components separately as Normalizing Flows. The log-likelihood of the original cosmological field can be recovered by summing over the log-likelihood of each wavelet term. This decomposition allows us to separate the information from different scales and identify distribution shifts in the data such as unknown scale-dependent systematics. The resulting likelihood analysis can not only identify these types of systematics, but can also be made optimal, in the sense that the Multiscale Flow can learn the full likelihood at the field without any dimensionality reduction. We apply Multiscale Flow to weak lensing mock datasets for cosmological inference, and show that it significantly outperforms traditional summary statistics such as power spectrum and peak counts, as well as novel Machine Learning based summary statistics such as scattering transform and convolutional neural networks. We further show that Multiscale Flow is able to identify distribution shifts not in the training data such as baryonic effects. Finally, we demonstrate that Multiscale Flow can be used to generate realistic samples of weak lensing data.

Keywords field-level inference · deep learning · normalizing flow · large-scale structure · weak lensing

1 INTRODUCTION

Numerous upcoming cosmological weak lensing surveys such as [Euclid](#), the [Vera Rubin Observatory](#) (Rubin), or [Nancy Grace Roman Space Telescope](#) (Roman) hold the promise of revolutionizing our understanding of the universe, its origins, content, and its future evolution. How to efficiently extract the maximum amount of cosmological information from these data is a long-standing question in large-scale structure (LSS) analysis. Due to the high-order correlations induced by nonlinear gravitational effects, the late-time cosmological fields are highly non-Gaussian with no tractable likelihood functions. Extracting information from these non-Gaussian fields has been mainly attempted through a limited set of summary statistics, with the most popular ones being the N-point correlation functions [e.g., 1, 2, 3, 4, 5]. However, while the two-point function is a natural choice even in the nonlinear regime, higher-order correlation functions are significantly more difficult to use due to the large number of statistical coefficients, large variance and high sensitivity to outliers [6]. Numerous other statistics have been proposed, including correlation functions on transformed or marked fields [7, 8], peak counts [9, 10], void statistics [11, 12], Minkowski functionals [13], scattering transform coefficients [14, 15], statistics learned by convolutional neural networks (CNNs) and other NNs [16, 17, 18, 19], and many others. These analyses have the same underlying issues of summary statistics being ad-hoc and potentially sub-optimal. They require building effective likelihood functions from summary statistics using multi-variate Gaussian or Simulation-Based Inference (SBI) methods [20], which can be costly when the number of summaries is large. An alternative approach is using the reconstruction of initial conditions and estimating the field-level likelihood function by marginalizing over all possible initial conditions using a variety of methods such as sampling or optimization

[21, 22, 23, 24, 25]. These methods are expensive because they perform reconstructions or sampling of 3-dimensional fields. They are also not well matched to the problem when the data is 2-dimensional, such as weak lensing.

Recently, Dai & Seljak [26] proposed directly learning the field-level data likelihood with Normalizing Flows (NFs). This approach does not require compressing the data into a low-dimensional summary statistic, and instead tries to extract all the information in the data from the field-level likelihood. Unlike the 3-d reconstructions, this approach does not require evaluating the high dimensional integral, and computes the likelihood function in a single forward pass of the flow network. Unlike SBI, it uses field level likelihood instead of summary statistics, performing Simulation Based Likelihood Inference (SBLI). To reduce the degrees of freedom when modeling the high-dimensional likelihood of the data they enforce translation and rotation symmetry into the NF. The resulting Translation and Rotation Equivariant Normalizing Flow (TRENF) agrees well with the analytical solution on Gaussian Random Fields, and it leads to significant improvement over the standard power spectrum analysis on nonlinear matter fields from N-body simulations [26]. Similarly, NFs with different architectures have been applied to neutral Hydrogen (HI) maps for fast sample generation and cosmological inference [27, 28].

Despite the differences in these LSS analysis methods, they all face the same challenge of robustness: how do we know which information is reliable, and which is not, if it is corrupted by effects that are ignored or inaccurately modeled? How do we detect distribution shifts in the actual data that were not in the training data? For example, most of these methods require accurate predictions from simulations, yet different hydrodynamical simulations and baryon models are not quite consistent with each other [29, 30]. Villaescusa-Navarro et al. [31] train CNNs

to predict cosmological parameters from gas temperature maps. They find that their model, trained using IllustrisTNG simulations [32], fails dramatically when applied to gas maps produced by SIMBA simulations [33], due to the different subgrid models used in these two simulations. While marginalizing over the baryon parameters, subgrid models and various systematic effects are helpful and necessary, there is no guarantee that current baryon and systematic models span all potential realistic scenarios.

One way to mitigate the impact of such modeling uncertainties is by separation of scales, with very small-scale information likely being contaminated by many astrophysical nuisance effects and observation systematics, and large-scale information likely being more robust. This strategy is widely used in current cosmological survey analyses of power spectrum or correlation function, for example by directly removing the small-scale information with scale cuts [e.g., 34, 35, 36], or by performing consistency checks between different scales [37]. The ability to perform a scale-dependent analysis is viewed as a distinct advantage of power spectrum or correlation function analysis when compared to other statistics.

In this paper, we apply the scale separation idea to the field-level likelihood modeling with NFs. Specifically, we use a set of scale-separated basis functions to represent the pixelized data, and decompose the data likelihood function into the contributions from different scales. Performing consistency checks between different scales enables us to decide what scale to include and what to exclude. While the Fourier basis is theoretically sound and widely used in such analysis, its kernels are not local in pixel space and require additional procedures in the presence of survey masks [26]. In this work we use wavelet basis, which is localized in both real space and Fourier space, allowing us to easily handle the survey mask and to separate the signals from different physical scales. Such decomposition is also known as Multiresolution Analysis (MRA) in image processing. Furthermore, our hierarchical analysis also combines likelihood information from different scales to achieve optimality in the limit of sufficient training data.

2 MULTIREOLUTION ANALYSIS WITH FAST WAVELET TRANSFORM

In this section we briefly introduce Multiresolution Analysis (MRA), which hierarchically decomposes the data into components at different scales, allowing us to separate the information from different scales and study them individually. This is particularly beneficial for cosmological analysis, since on large scales the universe can be modeled with simple physics and the data analysis is robust, while on small scales modeling the structure formation is harder due to nonlinear gravitational and astrophysical effects.

MRA is usually performed with Fast Wavelet Transform (FWT) [38]. While similar in concept to the Fourier basis, wavelet bases are constructed to be localized spatially, which is beneficial when analyzing maps with irregular footprints. Wavelet transform has been widely used in astronomical image processing [39] and statistical description of cosmological fields [14, 15]. In this work, we focus on decimated wavelet transform, which

preserves the dimensionality of the data and can be viewed as a special kind of NF transforms.

The basic idea of FWT is to recursively apply low-pass filters (also called scaling functions) and high-pass filters (also called wavelet functions) to the data. In each iteration, the data x_{2^n} with resolution 2^n is decomposed into a low-resolution approximation $x_{2^{n-1}}$, and detail coefficients of the remaining signal $x_{2^{n-1}}^d$:

$$x_{2^{n-1}} = (\phi * x_{2^n}) \downarrow 2 \quad (1)$$

$$x_{2^{n-1}}^d = (\psi * x_{2^n}) \downarrow 2 \quad (2)$$

where ϕ is the low pass filter (scaling function), ψ is the high pass filter (wavelet function), $*$ is the convolution operation, and $\downarrow 2$ is the operator to downsample the data by a factor of 2: $(x \downarrow 2)_{i,j} = x_{2i,2j}$. This is equivalent to a convolution with stride 2. For a 2D map x_{2^n} , we have three high pass filters to match the dimensionality, and the dimension of $x_{2^{n-1}}^d$ is $3 \times 2^{n-1} \times 2^{n-1}$. Then the low-resolution data $x_{2^{n-1}}$ is passed to the next iteration and treated as the input for further decomposition. Note that this decomposition is bijective and in each iteration the input data can be reconstructed with the inverse wavelet transform.

In this work, we use Haar wavelet [40], the simplest and the most spatially localized wavelet function. Its scaling function and wavelet function can be represented by the following 2×2 kernel in real space:

$$\phi = \frac{1}{4} \begin{bmatrix} 1 & 1 \\ 1 & 1 \end{bmatrix}, \psi_1 = \frac{1}{2} \begin{bmatrix} 1 & 1 \\ -1 & -1 \end{bmatrix}, \quad (3)$$

$$\psi_2 = \frac{1}{2} \begin{bmatrix} 1 & -1 \\ 1 & -1 \end{bmatrix}, \psi_3 = \begin{bmatrix} 1 & -1 \\ -1 & 1 \end{bmatrix}, \quad (4)$$

where we have scaled the scaling function such that $x_{2^{n-1}}$ is exactly the low-resolution version of x_{2^n} by taking the average of every 2×2 patch. The localized kernel of the Haar wavelet allows us to handle the survey mask easily, but our method can be generalized to other more complicated wavelet transforms, e.g., Daubechies wavelets [41].

With MRA, the log-likelihood of a map x_{2^n} with resolution 2^n can be rewritten into an auto-regressive form as

$$\begin{aligned} \log p(x_{2^n} | y) &= \log p(x_{2^{n-1}}, x_{2^{n-1}}^d | y) \\ &= \log p((x_{2^{n-1}} | y) + \log p(x_{2^{n-1}}^d | x_{2^{n-1}}, y) \\ &= \log p(x_{2^{n-2}} | y) + \log p(x_{2^{n-2}}^d | x_{2^{n-2}}, y) \\ &\quad + \log p(x_{2^{n-1}}^d | x_{2^{n-1}}, y) \\ &= \dots \\ &= \log p(x_{2^k} | y) + \sum_{m=k}^n \log p(x_{2^m}^d | x_{2^m}, y), \end{aligned} \quad (5)$$

where 2^k is the scale where we stop the decomposition, and k can be any integer between 0 and n . In practice, we can choose k such that it corresponds to the scale that either has extracted all the information from the data, or is large enough not to be affected by unknown small-scale systematic effects.

3 MULTISCALE FLOW

3.1 Normalizing Flows

Flow-based models provide a powerful framework for density estimation [42, 43] and sampling [44]. These models map the

data x to latent variables z through a sequence of invertible transformations $f = f_1 \circ f_2 \circ \dots \circ f_n$, such that $z = f(x)$ and z is mapped to a base distribution $\pi(z)$. The base distribution $\pi(z)$ is normally chosen to be a Gaussian with zero mean and unit variance, $\pi(z) = \mathcal{N}(0, I)$. The probability density of data x can be evaluated using the change of variables formula:

$$\begin{aligned} p(x) &= \pi(f(x)) \left| \det \left(\frac{\partial f(x)}{\partial x} \right) \right| \\ &= \pi(f(x)) \prod_{i=1}^n \left| \det \left(\frac{\partial f_i(x)}{\partial x} \right) \right|. \end{aligned} \quad (6)$$

To sample from $p(x)$, one first samples latent variable z from $\pi(z)$, and then transform variable z to x through $x = f^{-1}(z)$. The transformation f is usually parametrized with neural networks f_ϕ , and the parameters ϕ are normally estimated using Maximum Likelihood Estimation (MLE):

$$\phi^* = \arg \max_{\phi} \frac{1}{N} \sum_{i=1}^N \log p_\phi(x_i), \quad (7)$$

where the data likelihood $p(x)$ is given by Equation 6. The MLE solution minimizes the Kullback-Leibler (KL) divergence between the model distribution $p_\phi(x)$ and the true data distribution. The parameterization of f must satisfy the requirements that the Jacobian determinant $\det(\frac{\partial f_i(x)}{\partial x})$ is easy to compute for evaluating the density, and the transformation f_i is easy to invert for efficient sampling.

In cosmological analysis we are interested in the likelihood function $p(x|y)$, which can be estimated using conditional Normalizing Flows (NFs). In conditional NFs the flow transformation is dependent on the conditional parameters y , i.e., $f = f_{\phi,y}$. We discuss below how we parametrize and train the conditional flow $f_{\phi,y}$.

3.2 Multiscale Flow

With the likelihood decomposition Equation 5, our task now is to build NFs to model different likelihood terms separately. For simplicity, we will drop the subscript 2^m in this section, and simply refer to the conditional likelihood term $\log p(x_{2^m}^d | x_{2^m}, y)$ as $\log p(x^d | x, y)$. The model described here is similar to Wavelet Flow [45], even though they are developed independently. Following Glow [44], our flow transformation $f(x|y)$ consists of multiple block flows, where each block consists of an actnorm, an invertible 1×1 convolution, and an affine coupling layer.

Actnorm: The actnorm layer applies an affine transformation per channel, similar to batch normalization [46], but its scale and bias parameters are initialized such that the output has zero mean and unit variance per channel given an initial minibatch of data, and then these parameters are treated as regular trainable parameters.

Invertible 1×1 convolution: The invertible 1×1 convolution is a learnable $C \times C$ matrix (where C is the number of channels) that linearly mixes different channels.

Affine coupling: The affine coupling layer firstly splits the data x^d to x^{d1} and x^{d2} based on the channels, and then applies pixel-wise affine transformation to x^{d2} , with scale and bias given by x^{d1} :

$$(\log s, t) = \text{CNN}(x^{d1}, x, y) \quad (8)$$

$$z^{d2} = \exp(\log s) \cdot x^{d2} + t, \quad (9)$$

where $\log s$ and t are scale and bias coefficient maps with the same dimensionality as x^{d2} , and CNN is a learned function parametrized by a convolutional neural network. The dependence of conditional parameter y is modeled by introducing gating into CNN, i.e., each channel of CNN is scaled by a value between 0 and 1 which is determined by parameter y . This gating allows the conditional variable y to determine the relative weights between different features (channels). The output of the affine coupling layer is the concatenation of x^{d1} and z^{d2} . In other words, the affine coupling layer applies an affine transformation to x^{d2} and leaves x^{d1} unchanged. In this paper, we consider 2D maps, so at each scale x^d contains 3 maps (channels). We set the first channel to be x^{d1} , and the other two channels to be x^{d2} .

To summarize, a Multiscale Flow consists of multiple NFs, and each NF models one term of the likelihood decomposition (Equation 5) separately. The large-scale term $\log p(x_{2^k}|y)$ is modeled by q flow blocks, and each other term $\log p(x_{2^m}^d | x_{2^m}, y)$ is modeled with p flow blocks, where p and q are hyperparameters in the model. Note that all of these NFs can be trained independently in parallel to speed up the training process.

3.3 Training

Following Dai & Seljak [26], we adopt a two-stage training strategy in this work: we first train the NF with the generative loss, which minimizes the negative log-likelihood and is the standard loss function of NF (Equation 7 with conditional variable y):

$$\mathcal{L}_g = -\frac{1}{N} \sum_{i=1}^N \log p(x_i|y_i). \quad (10)$$

The generative loss is suitable for sampling and density estimation, but may lead to a biased or overconfident posterior [26]. To solve this issue they propose further optimizing the posteriors by training the model with the discriminative loss, $\mathcal{L}_d = -\frac{1}{N} \sum_{i=1}^N \log p(y_i|x_i) = -\frac{1}{N} \sum_{i=1}^N [\log p(x_i|y_i) + \log p(y_i) - \log p(x_i)]$, where the evidence $p(x)$ is estimated using Importance Sampling (IS): $\log p(x) \approx \log \frac{1}{M} \sum_{y_j \sim q(y|x)} \frac{p(x|y_j)p(y_j)}{q(y_j|x)}$, and $q(y|x)$ is chosen to be a Gaussian distribution with learned mean and fixed covariance matrix. However, we find that IS becomes inefficient when the number of parameters y gets large and when the posterior becomes non-Gaussian. Furthermore, training on posteriors may not always solve the overconfidence problem [47].

In this work, we propose adding another loss term that forces the posteriors to be well-calibrated. Our proposed loss term is based on the notion that properly calibrated Bayesian posteriors have to result in the correct frequency of events. If the prior is flat the posterior is entirely determined by the likelihood. We thus enforce that the average likelihood over the training data equals the likelihood averaged over the posterior. The loss is defined as

$$\begin{aligned} \tilde{\mathcal{L}}_d &= \frac{1}{N} \sum_{i=1}^N \log p(x_i|y_i) - \int p(y|x_i) \log p(x_i|y) dy \\ &\approx \frac{1}{N} \sum_{i=1}^N \log p(x_i|y_i) - \frac{1}{M} \sum_{y_j \sim p(y|x_i)} \log p(x_i|y_j). \end{aligned} \quad (11)$$

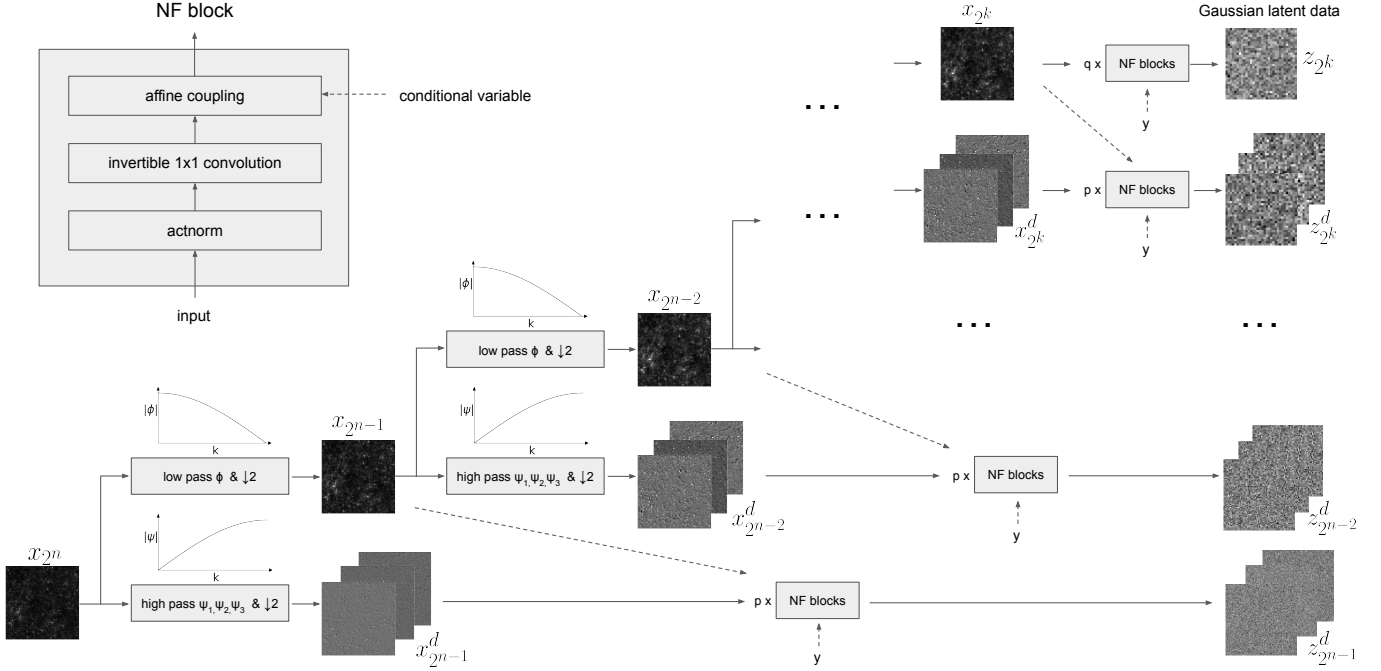


Figure 1: Illustration of Multiscale Flow model. The input map x_{2^n} with resolution 2^n is iteratively processed with a set of low pass filters (ϕ), high pass filters (ψ_1, ψ_2, ψ_3) and downsampling ($\downarrow 2$), resulting in a series of detailed maps $x_{2^{n-1}}^d, x_{2^{n-2}}^d, \dots, x_{2^k}^d$ and an approximation map x_{2^k} . These maps are then transformed by several NF blocks to Gaussian latent maps $z_{2^{n-1}}^d, z_{2^{n-2}}^d, \dots, z_{2^k}^d, z_{2^k}$, where each NF block is composed of an actnorm layer, an invertible 1×1 convolution, and an affine coupling layer (Equation 8, 9), as shown on the top left of this figure. The NF transformation is conditioned on the conditional variable y and approximation maps, which are represented by dashed arrows in the illustration. The log-likelihood of the input map x_{2^n} can be calculated with Equation 5.

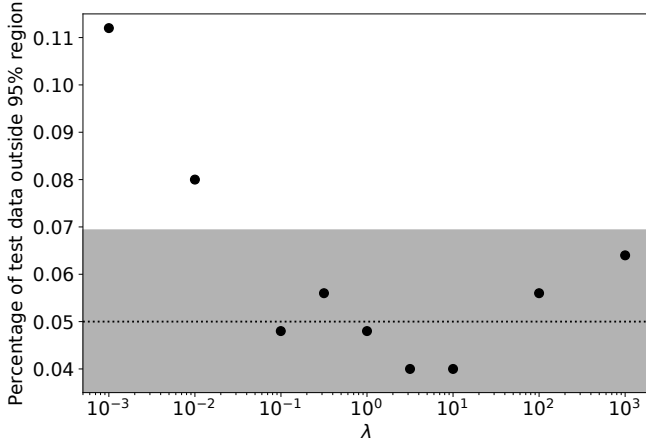


Figure 2: Percentage of test data that fall outside 95% confidence region for different λ values. A perfectly calibrated posterior has 5% outliers. The shaded region shows the uncertainty due to finite number of test data. This measurement is made on weak lensing maps with 64^2 resolution and $n_g = 30 \text{arcmin}^{-2}$ galaxy density.

After the generative training we add this loss to the generative loss with a hyperparameter λ , $\mathcal{L} = \frac{1}{1+w\lambda} \mathcal{L}_g + \frac{w\lambda}{1+w\lambda} \tilde{\mathcal{L}}_d$, where $w = \frac{d_x}{d_y}$ is a prefactor to balance the dimension difference between the data and the parameter space, and we divide the loss by $1 + w\lambda$

to normalize the weights. In Figure 2 we show the percentage of outliers in our posterior analysis with different λ values. For very small λ the posterior is too narrow (underestimated errors) and the loss is dominated by the first loss term (generative loss). For $\lambda > 0.1$ the posterior is well calibrated due to the second term $\tilde{\mathcal{L}}_d$. In this paper, we use large λ to calibrate the posterior, which leads to a slightly conservative calibration (Table 3 and Figure 2).

In the second line of Eq. 11 we replaced the integral with Monte Carlo estimates, which require samples from the posterior $p(y|x_i)$. We obtain the posterior samples by running a Hamiltonian Monte Carlo (HMC) sampler [48] before the hybrid training. In this paper, we generate $M = 5 - 10$ HMC samples for each data with 200 HMC steps. These samples are saved, and then updated with 5 - 20 HMC steps every epoch of training. An advantage of $\tilde{\mathcal{L}}_d$ compared to \mathcal{L}_d is that instead of evaluating the evidence term $\log p(x) = \log \int p(x|y)p(y)dy$, we now evaluate $\int \log p(x|y)p(y|x)dy$. The estimation of the former usually comes with a large variance, while the latter can be estimated with only a few HMC samples.

4 RESULTS

4.1 Cosmological constraints from noisy weak lensing maps

We apply Multiscale Flow to $3.5 \times 3.5 \text{deg}^2$ mock weak lensing convergence maps [50] for field-level inference. We decom-

Table 1: Comparison of the constraining power between different methods. The figure of merit is measured by the reciprocal of the 1σ confidence area on the (Ω_m, σ_8) plane, using a $3.5 \times 3.5 \text{ deg}^2$ convergence map.

Method	$n_g = 10 \text{arcmin}^{-2}$	$n_g = 30 \text{arcmin}^{-2}$	$n_g = 100 \text{arcmin}^{-2}$
Multiscale Flow $p(x_{512} y)$	149	375	957
Multiscale Flow $p(x_{256} y)$	143	353	858
Multiscale Flow $p(x_{128} y)$	108	281	706
Multiscale Flow $p(x_{64} y)$	72	175	391
power spectrum	30 (30)	52 (51)	81 (79)
peak count	(40)	(85)	(137)
CNN	(44)	(121)	(292)
scattering transform $s_0 + s_1 + s_2$	($\lesssim 50$)	($\lesssim 140$)	($\lesssim 329$)

1. Unless specified with Multiscale Flow, the analysis of other approaches are performed on maps with resolution 512^2 .
2. The numbers in parenthesis are estimated using maps with 1 arcmin Gaussian smoothing. We expect this smoothing to have little effect on constraining power estimation, because the small-scale modes are dominated by shape noise. This is also explicitly verified in the case of power spectrum, where we show FoM with and without smoothing.
3. The FoM of the scattering transform is estimated using the Fisher matrix, which is an upper limit of the true FoM according to the Cramér-Rao inequality. It has been shown that Fisher forecast could potentially overestimate the 1D parameter constraints by a factor of 2, due to the non-Gaussian distribution of the statistics. [49].

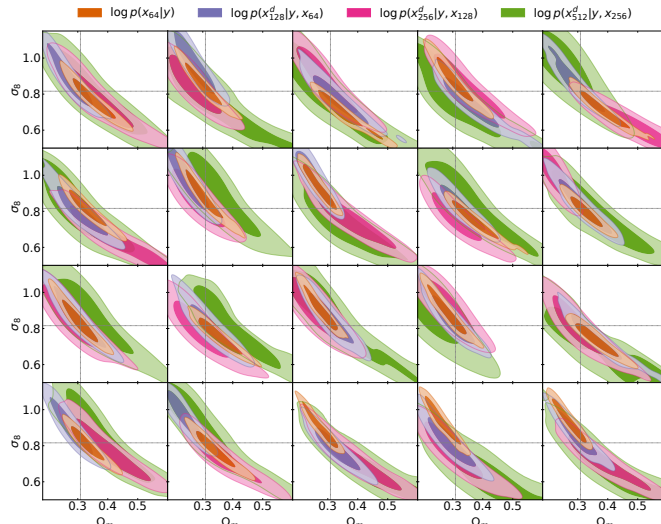


Figure 3: Multiscale Flow posterior comparison of different scales on 20 test data with galaxy number density $n_g = 30 \text{arcmin}^{-2}$.

pose the 512^2 resolution map to four scales, with likelihood decomposition

$$\log p(x_{512}|y) = \log p(x_{64}|y) + \log p(x_{64}^d|x_{64}, y) + \log p(x_{128}^d|x_{128}, y) + \log p(x_{256}^d|x_{256}, y). \quad (12)$$

The posterior comparison of different scales on 20 test maps with galaxy number density $n_g = 30 \text{arcmin}^{-2}$ is shown in Figure 3. The posterior constraints of all scales are consistent with the true cosmological parameters, which are shown as black lines. The constraining power of Multiscale Flow of different galaxy shape noise levels is shown in Table 1. We list the figure of merit (defined as the reciprocal of the 1σ confidence area on the (Ω_m, σ_8) plane) of maps with different resolutions, and compare them with summary statistics power spectrum, peak count, scattering transform [14], and statistics learned by CNNs [50]. Multiscale Flow achieves the best performance among all

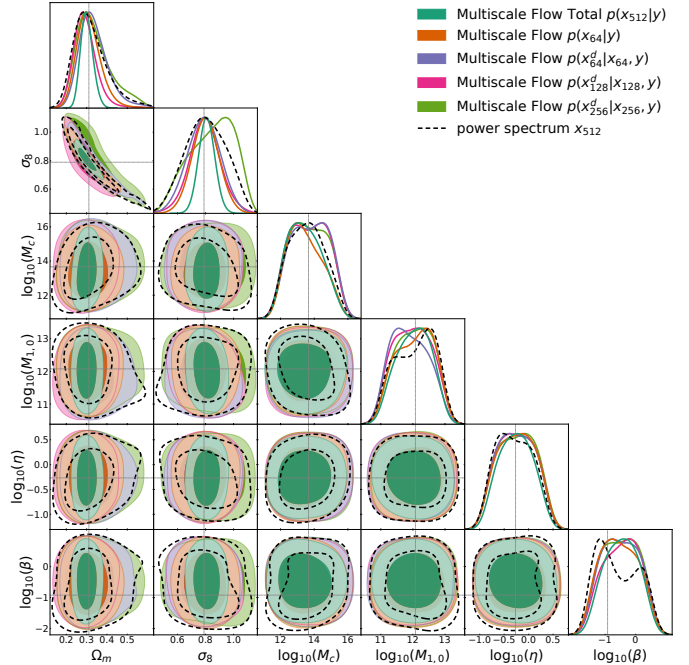


Figure 4: Comparison of posterior distributions between different scales of Multiscale Flow and power spectrum on a $3.5 \times 3.5 \text{deg}^2$ convergence map with $n_g = 20 \text{arcmin}^{-2}$.

methods, outperforming power spectrum by factors of 5, 7 and 12 on galaxy densities $n_g = 10, 30, 100 \text{arcmin}^{-2}$, respectively. Multiscale Flow also achieves two to three higher constraining power when compared to peak counts, CNN, and scattering transform.

4.2 Impact of baryons

Next, we apply Multiscale Flow to mock weak lensing maps with baryonic physics included [51]. Similar to the previous experiment, these maps also have a resolution of 512^2 , and we adopt the same likelihood decomposition as Equation 12. We

Table 2: Similar to Table 1, with baryonic effects.

	Method	$n_g = 10\text{arcmin}^{-2}$	$n_g = 20\text{arcmin}^{-2}$	$n_g = 50\text{arcmin}^{-2}$	$n_g = 100\text{arcmin}^{-2}$
Fix baryon parameters at fiducial values	Multiscale Flow $p(x_{512} y)$	166	310	617	1072
	Multiscale Flow $p(x_{256} y)$	164	297	558	947
	Multiscale Flow $p(x_{128} y)$	124	214	415	704
	Multiscale Flow $p(x_{64} y)$	81	136	247	387
	power spectrum	41(41)	61 (58)	95(87)	127(111)
Marginalize over baryon parameters	CNN	-	(~ 93)	(~ 146)	(~ 194)
	Multiscale Flow $p(x_{512} y)$	149	220	362	521
	Multiscale Flow $p(x_{256} y)$	147	213	341	494
	Multiscale Flow $p(x_{128} y)$	112	166	269	398
	Multiscale Flow $p(x_{64} y)$	75	113	183	259
	power spectrum	34(33)	48(48)	68(65)	84 (78)
	CNN	-	(~ 77)	(~ 109)	(~ 136)

1. When fixing the baryon parameters at fiducial values, the FoM of CNN are estimated from Lu et al. [51]. Lu et al. [51] estimated the 1σ area of a 1500deg^2 survey, and we scale their results by the area ratio for a direct comparison with our experiments.
2. For marginalizing over baryon parameters, simply rescaling the results of Lu et al. [51] by the area ratio underestimates the constraining power of CNN, due to the prior bounds of baryon parameters. Instead, we estimate its FoM by $\frac{\text{FoM}_{\text{PS},\text{marginal}}}{\text{FoM}_{\text{PS},\text{fiducial}}} \text{FoM}_{\text{CNN},\text{fiducial}}$.

Table 3: Empirical coverage probability of posteriors from different methods, after marginalizing over baryon parameters. We report the percentage of test data that falls within the 68% confidence region and the 95% confidence region. A perfectly calibrated posterior should have 68% and 95% test data that fall in these two regions, respectively.

Method	$n_g = 10\text{arcmin}^{-2}$	$n_g = 20\text{arcmin}^{-2}$	$n_g = 50\text{arcmin}^{-2}$	$n_g = 100\text{arcmin}^{-2}$
Multiscale Flow $p(x_{512} y)$	72.8%, 96.8%	74.4%, 95.2%	73.6%, 97.6%	66.4%, 97.6%
Multiscale Flow $p(x_{256} y)$	70.4%, 96.0%	76.8%, 95.2%	74.4%, 97.6%	68.8%, 96.8%
Multiscale Flow $p(x_{128} y)$	76.0%, 96.0%	74.4%, 97.6%	76.0%, 97.6%	73.6%, 96.8%
Multiscale Flow $p(x_{64} y)$	80.8%, 95.2%	70.4%, 94.4%	72.0%, 95.2%	74.4%, 95.2%

have 6 physical parameters in total, i.e., cosmological parameters Ω_m and σ_8 , and 4 baryon parameters [52]. The posterior distributions of Multiscale Flow and power spectrum of a test data with $n_g = 20\text{arcmin}^{-2}$ are shown in Figure 4. In Table 2 we compare the constraining power of Multiscale Flow, power spectrum, and CNN [51] on (Ω_m, σ_8) plane. With the presence of baryon physics, Multiscale Flow has 4 – 6 times higher constraining power on cosmological parameters when compared to the power spectrum. It also outperforms CNN by a factor of 3-5.

Unfortunately, due to the small area of the lensing map, all these methods cannot constrain baryon parameters very well (see also Figure 5 of Lu et al. [51] for CNN constraints), and the posterior is dominated by the prior bounds, especially in the cases of high shape noise. Therefore, marginalizing the baryon parameters has a small impact on the Figure of Merit. With smaller shape noise and a more powerful model, the posterior becomes more dominated by likelihood rather than the prior, and the degradation of FoM when marginalizing over the baryon parameters gets larger. This explains why the degradation of baryon marginalization is larger for Multiscale Flow compared to the power spectrum, and why the degradation is larger in high galaxy number density cases. However, it is important to recognize that with better statistical power, and simpler baryonic models, we expect field level inference to be able to break the degeneracies between baryonic and cosmological parameters.

We apply Multiscale Flow to test data with fiducial parameters, and in Table 3 we report the percentage of test data with true cosmological parameters to fall in 68% and 95% confidence regions. In most cases the percentages are larger than the 68% and 95% expectation, suggesting that our posterior constraint is conservative.

4.3 Identifying distribution shifts

Identifying distribution shifts from unknown effects that are present in the data, but not in the training simulations, is one of the great challenges of modern Machine Learning. Here we propose two different methods to identify such shifts. In the first approach, we evaluate the likelihood value of test data at MAP $\log p(x|y_{\text{MAP}})$ and compare it with the distribution of training data. If it is smaller than the typical likelihood values of training data, it is likely not in the typical set of training distribution. In the second approach, we use consistency of information as a function of scale to identify such shifts. Specifically, we evaluate

$$\Delta \log p(x_m|y) = \log p(x_m|y_{\text{MAP}}) - \log p(x_m|y_{\text{MAP},m}), \quad (13)$$

where x_m is the data of a specific scale, $y_{\text{MAP},m} = \arg \max_y \log p(y|x_m)$ is the MAP of this scale, and y_{MAP} is the MAP of all the scales. If there are scale-dependent systematic effects that bias the posterior in different ways, we expect y_{MAP}

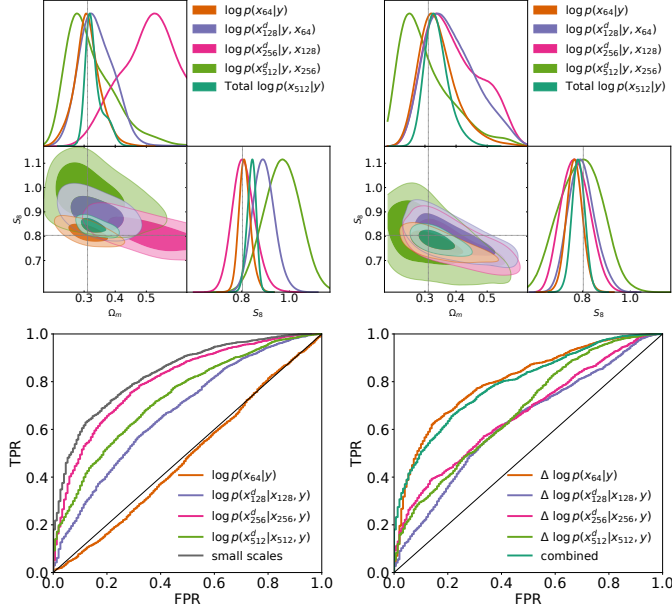


Figure 5: Top panel: scale-dependent posterior analysis of a baryon-corrected convergence map using Multiscale Flow trained on dark-matter-only maps (left), and Multiscale Flow trained on BCM maps (right). Bottom panel: ROC curve of identifying distribution shift with $\log p$ (left) and $\Delta \log p$ (right). The "small scales" in the lower left panel represent combining the three small scale terms. In these experiments, we consider 30arcmin^{-2} galaxy shape noise.

and $y_{\text{MAP},m}$ to be quite different, and $\Delta \log p(x_m|y)$ should be smaller compared to those of training data.

As a simple example, we train the Multiscale Flow with dark-matter-only convergence maps [50], and apply the model to convergence maps with baryon physics included [51]. We show the posterior distributions from different scales in the upper left panel of Figure 5. The baryon physics modifies the matter distribution on small scales and biases the posterior constraints from small scales. In this case, naively combining all of the scales leads to a posterior constraint that is 2σ biased (dark green contour). The inconsistency of posterior between different scales suggests a presence of unknown systematics (baryon physics) that is not modeled in the training data. If we remove the small-scale information (because we believe the large scales are less likely to be affected by systematics), we can recover an unbiased constraint of cosmological parameters (orange contour). As a comparison, in the upper right panel, we show the posteriors from Multiscale Flow trained using maps with baryon physics. There is no distribution shift in this case and the information from the different scales is consistent.

In the bottom panel of Figure 5, we show the ROC curve of identifying this distribution shift with $\log p$ and $\Delta \log p$. As expected, the likelihood of large-scale term $\log p(x_{64}|y)$ cannot tell the difference between with and without baryon physics, while the likelihood of small-scale terms can be used for detecting the shifts. By combining all the small-scale terms, we get the best performance with AUROC of 0.84. We also find that $\Delta \log p$ work equally well in this task. In this case the large-scale term

$\Delta \log p(x_{64}|y)$ achieves the best performance with AUROC of 0.80, because the small-scale constraints bias y_{MAP} away from $y_{\text{MAP},64}$. The two methods are essentially independent, and combining them further improves OoD detection. These maps have a small area ($3.5 \times 3.5\text{deg}^2$), and the 2048 test data used in this experiment span a wide range of baryon parameters, of which many are likely indistinguishable from the no baryons given the sampling variance between the maps. We expect our OoD detection methods will work even better for sky surveys with larger areas and for models where baryonic effects are more significant.

4.4 Sample generation and super-resolution

We show an example of sample generation with Multiscale Flow in Figure 6. The process can also be viewed as iterative super-resolution of the low-resolution samples. In Figure 7 we show that Multiscale Flow samples and test data agree well in terms of the power spectrum and pixel probability distribution function. This demonstrates that Multiscale Flow samples can be used in lieu of expensive N-body simulations and ray tracing as a fast generator of mock data.

5 DISCUSSION

In this paper, we develop a Multiscale Flow model for field-level cosmological inference. Multiscale Flow tries to model the likelihood function of the cosmological field without any dimension reduction. If the field is learned perfectly, the resulting likelihood analysis becomes optimal. On mock weak lensing convergence dataset we demonstrate that the constraining power of Multiscale Flow outperforms the power spectrum in terms of Figure of Merit by factors of 4 - 6, depending on the noise level, and outperforms CNN by a factor 3 for the most realistic case with a noise level of 20arcmin^{-2} and with baryon marginalization.

Multiscale Flow enables field-level scale-dependent posterior analysis, which helps the identification of scale-dependent systematics that are not accurately modeled in training simulations. We demonstrate that it is able to identify distribution shifts on weak lensing maps with baryonic physics if the model is trained with dark-matter-only maps.

In this paper, our main focus is optimal and robust field-level likelihood analysis, but we also show that Multiscale Flow can be used for fast sample generation and super-resolution, replacing the need for expensive N-body simulations and ray tracing. We expect many other applications of Multiscale Flow, such as 21cm and other intensity maps, weak lensing maps, projected galaxy clustering, X-ray and thermal SZ maps, etc. Multiscale Flow can also be used to model 3D galaxy fields or 1D spectrum data like Lyman alpha forest.

Multiscale Flow can be generalized to model maps with multiple channels $x_{2^n} = \{x_{2^n}^c\}_{c=1}^C$, where c represents the index of channels, and C is the total number of channels. Here the channels could represent different tomographic bins of cosmic shear analysis, or different tracers on the same area of the sky, such as galaxies and weak lensing. We can still use Equation 5 to decompose the likelihood of input maps with multiple channels, and each term

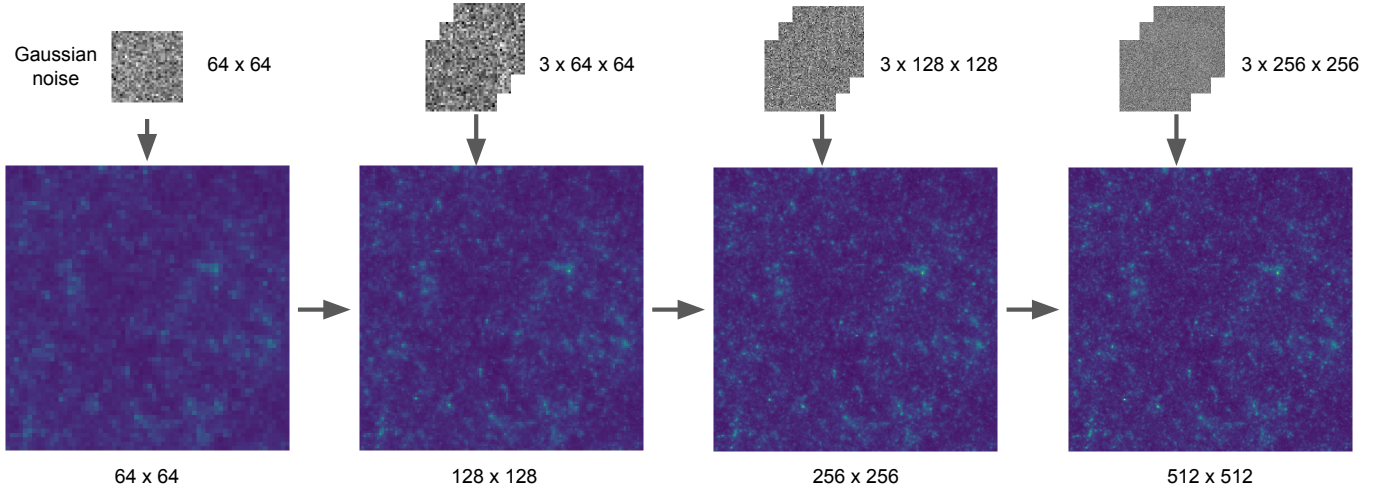


Figure 6: Illustration of Multiscale Flow sample generation (the reverse of Figure 1). The sample of the lowest resolution is first generated, and then small-scale information is gradually added. This process can also be viewed as super-resolution.

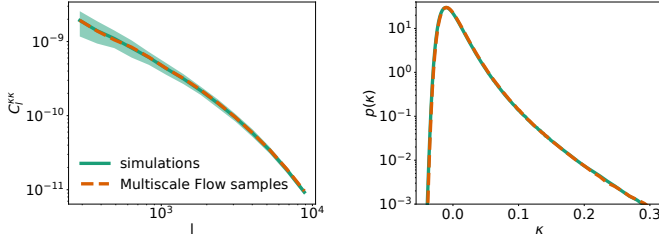


Figure 7: Comparison of the power spectrum (left) and pixel probability distribution function (right) between simulations and Multiscale Flow samples at fiducial cosmology.

can be further decomposed with

$$\log p(x_{2^k}|y) = \sum_{c=1}^C \log p(x_{2^k}^c|x_{2^k}^1, \dots, x_{2^k}^{c-1}, y),$$

$$\log p(x_{2^m}^d|x_{2^m}, y) = \sum_{c=1}^C \log p(x_{2^m}^{d,c}|x_{2^m}^{d,1}, \dots, x_{2^m}^{d,c-1}, x_{2^m}, y),$$

which allows us to check for consistency between different channels.

Multiscale Flow can also be generalized to model maps with survey masks. Following the strategy developed in [26], one can first sample noise at the masked region, and then introduce position-dependent flow transformation to the model to learn the effect of survey mask. It can thus be applied to realistic surveys such as Hyper Suprime-Cam [53], Euclid [54], or Vera C. Rubin Observatory Legacy Survey of Space and Time [55] for their robust and optimal analysis.

MATERIALS AND METHODS

Dark-matter-only weak lensing maps

The weak lensing convergence maps from Gupta et al.[19] are generated from a suite of 75 N-body simulations with spatially flat Λ CDM cosmologies. Each simulation differs in cosmological parameters Ω_m and σ_8 , while the other cosmological parameters are fixed at $\Omega_b = 0.046$, $h = 0.72$ and $n_s = 0.96$. The two

cosmological parameters Ω_m and σ_8 are sampled non-uniformly with density increases towards $\Omega_m = 0.26$ and $\sigma_8 = 0.8$. Each simulation evolves 512^3 dark matter particles in a $240h^{-1}$ Mpc box with N-body code gadget-2 [56]. A series of snapshots are saved between redshifts $0 < z < 1$ such that adjacent snapshots are separated by $80h^{-1}$ Mpc in comoving distance.

Weak lensing convergence maps with field of view 3.5×3.5 deg² are then generated by ray-traced the snapshots of N-body simulations to redshift $z = 1$ with multiple lens plane algorithm [57]. 512 pseudo-independent maps are created from each simulation by randomly rotating, flipping, and shifting the simulation snapshots. We refer the reader to Gupta et al.[19] for a detailed description of how these data were generated.

Following Ribli et al.[50], we downsample the maps from resolution 1024^2 to resolution 512^2 (~ 0.4 arcmin), and add Gaussian galaxy shape noise to the maps with a standard deviation

$$\sigma = \frac{\sigma_\epsilon}{\sqrt{2n_{\text{gal}}A_{\text{pixel}}}}, \quad (14)$$

where $\sigma_\epsilon = 0.4$ is the mean intrinsic ellipticity of galaxies and A_{pixel} the area of the pixel. For this dataset we consider three different galaxy densities: $n_g = 10$ arcmin⁻², $n_g = 30$ arcmin⁻² and $n_g = 100$ arcmin⁻². Ribli et al.[50] smooth the maps with a 1 arcmin Gaussian kernel to increase the signal-to-noise (S/N) ratio and removes the information at very small scales where baryonic physics alters the matter distribution. In our analysis, however, we do not smooth the noisy maps. This is because our Normalizing Flow models the likelihood function by mapping the convergence map to a Gaussian random field of the same dimensionality, implicitly assuming that the input map is full-ranked. With Gaussian smoothing, the small-scale modes of smoothed maps become degenerate and the probability distribution is no longer full-ranked, leading to model failure in our analysis.

Weak lensing maps with baryon

To study the impact of baryonic effects in our analysis, we also consider weak lensing convergence maps from Lu et al.[51].

These maps are generated from the same set of N-body simulations and ray-tracing algorithms as the dark-matter-only maps described above, and have the same resolution and field of view. The main difference is that the simulation snapshots are post-processed to include the baryonic effects. We briefly describe this post-processing step below and refer the reader to Lu et al.[58, 51] for more details.

Lu et al.[51] find all dark matter halos with mass $> 10^{12} M_{\odot}$ in the simulation snapshots, and replace the halo particles with spherically symmetric analytical halo profiles to characterize the matter distribution inside halos. The analytical halo profile is given by Baryon Correction Model [BCM, 52], which describes the halos with four components: the central galaxy (stars), bounded gas, ejected gas (due to AGN feedback), and relaxed dark matter. The masses and profiles of these four components are parametrized by four free parameters: M_c (the characteristic halo mass for retaining half of the total gas), $M_{1,0}$ (the characteristic halo mass for a galaxy mass fraction of 0.023), η (the maximum distance of the ejected gas from the parent halo), and β (the logarithmic slope of the gas fraction vs. the halo mass). This post-processing step removes the substructure and non-spherical shape of the halos, but it has been shown that these morphological differences between the simulated halos and spherical analytical profiles are not statistically significant when compared to the uncertainties of the power spectrum and peak counts in an HSC-like survey [58].

Lu et al.[51] create 2048 maps with different baryon parameters for each cosmology. They train CNN with the first 1024 maps, and use the other 1024 maps to measure the mean and covariance matrix of the learned statistics. In our analysis, we only use the first 1024 maps to train our Multiscale Flow and do not use the rest of the 1024 maps.

Similar to the preprocessed steps of the dark-matter-only maps (described in the previous section), we downsample the maps to resolution 512^2 , and add Gaussian shape noise (Equation 14). For this dataset we consider four galaxy densities: $n_g = 10 \text{ arcmin}^{-2}$, $n_g = 20 \text{ arcmin}^{-2}$, $n_g = 50 \text{ arcmin}^{-2}$ and $n_g = 100 \text{ arcmin}^{-2}$, to better compare our results with Lu et al.[51].

Multiscale Flow Hyperparameters

We use $p = 12$ block flows to model the large-scale term $\log p(x_{64}|y)$, and $q = 4$ block flows to model each of the three small-scale terms. The CNN in Equation 8 is chosen to be a convolutional residual neural network with 2 residual blocks and 64 hidden channels in the residual blocks.

Summary Statistics Analysis

In this paper, we compare the performance of Multiscale Flow with analysis based on summary statistics. We consider not only standard summary statistics such as power spectrum and peak count, but also novel statistics such as scattering transform and convolutional neural networks (CNNs).

Power Spectrum

We compute the power spectrum of the convergence maps using the publicly available LensTools package [59]. The power spectrum is calculated in 20 bins in the range $100 \leq l \leq 37500$

with logarithmic spacing, following the settings adopted in Ribli et al.[50] and Cheng et al.[14]. We take the logarithm of the power spectrum to be observable for parameter inference.

Peak Count

In Table 1, we take the peak count measurement from Ribli et al. [50], who identify the local maxima of convergence maps and measure the binned histogram of the peaks as a function of their κ value. They use 20 linearly spaced κ bins in total.

Scattering transform

Originally proposed by Mallat[60] as a tool to extract information from high-dimensional data, scattering transform has recently been applied to cosmological data analysis and shown improvement over the power spectrum in low noise regime [e.g., 14, 15, 61, 62]. For a given input field, the scattering transform first generates a group of new fields by recursively applying wavelet convolutions and modulus. The expected values of these fields are then defined as the scattering coefficients and used as the summary statistics. In this paper we compare our results directly to Cheng et al.[14], who estimate the constraining power of scattering transform using Fisher forecast on the same dataset.

Convolutional Neural Networks (CNN)

Several studies have explored using CNNs to construct summary statistics for cosmological inference [16, 18, 19, 50, 51, 63]. In this work we compare our results on dark-matter-only weak lensing maps with Ribli et al.[50], and compare our results with Lu et al.[51] on weak lensing maps with baryons. Ribli et al.[50] and Lu et al.[51] train CNNs to predict cosmological parameters from the same convergence maps used in this work. Then they view these predicted parameters as summary statistics, and build Gaussian likelihood on these statistics for inference.

ACKNOWLEDGEMENTS

We thank the Columbia Lensing group (<http://columbialensing.org>) for making their simulations available. B.D. thanks Xiangchong Li for helpful discussions on wavelet transform. This work is supported by U.S. Department of Energy, Office of Science, Office of Advanced Scientific Computing Research under Contract No. DE-AC02-05CH11231 at Lawrence Berkeley National Laboratory to enable research for Data-intensive Machine Learning and Analysis.

REFERENCES

- [1] P. J. E. Peebles. *The large-scale structure of the universe*. 1980.
- [2] P. J. E. Peebles and E. J. Groth. Statistical analysis of catalogs of extragalactic objects. V. Three-point correlation function for the galaxy distribution in the Zwicky catalog. *The Astrophysical Journal*, 196:1–11, February 1975. doi: 10.1086/153390.

[3] Emiliano Sefusatti, Martín Crocce, Sebastián Pueblas, and Román Scoccimarro. Cosmology and the bispectrum. *Physical Review D*, 74(2):023522, 2006.

[4] Elisabetta Semboloni, Tim Schrabback, Ludovic van Waerbeke, Sanaz Vafaei, Jan Hartlap, and Stefan Hilbert. Weak lensing from space: first cosmological constraints from three-point shear statistics. *Monthly Notices of the Royal Astronomical Society*, 410(1):143–160, 2011.

[5] Liping Fu, Martin Kilbinger, Thomas Erben, Catherine Heymans, Hendrik Hildebrandt, Henk Hoekstra, Thomas D Kitching, Yannick Mellier, Lance Miller, Elisabetta Semboloni, et al. Cfhtlens: cosmological constraints from a combination of cosmic shear two-point and three-point correlations. *Monthly Notices of the Royal Astronomical Society*, 441(3):2725–2743, 2014.

[6] Maurice George Kendall et al. The advanced theory of statistics. *The advanced theory of statistics.*, (2nd Ed), 1946.

[7] Mark C. Neyrinck, István Szapudi, and Alexander S. Szalay. Rejuvenating the Matter Power Spectrum: Restoring Information with a Logarithmic Density Mapping. *The Astrophysical Journal Letters*, 698(2):L90–L93, June 2009. doi: 10.1088/0004-637X/698/2/L90.

[8] Martin White. A marked correlation function for constraining modified gravity models. *Journal of Cosmology and Astroparticle Physics*, 2016(11):057, 2016.

[9] Bhuvnesh Jain and Ludovic Van Waerbeke. Statistics of Dark Matter Halos from Gravitational Lensing. *The Astrophysical Journal Letters*, 530(1):L1–L4, February 2000. doi: 10.1086/312480.

[10] Jan M. Kratochvil, Zoltán Haiman, and Morgan May. Probing cosmology with weak lensing peak counts. *Physical Review D*, 81(4):043519, February 2010. doi: 10.1103/PhysRevD.81.043519.

[11] Simon DM White. The hierarchy of correlation functions and its relation to other measures of galaxy clustering. *Monthly Notices of the Royal Astronomical Society*, 186(2):145–154, 1979.

[12] Alice Pisani, Elena Massara, David N. Spergel, David Alonso, Tessa Baker, Yan-Chuan Cai, Marius Cautun, Christopher Davies, Vasiliy Demchenko, Olivier Doré, Andy Goulding, Mélanie Habouzit, Nico Hamaus, Adam Hawken, Christopher M. Hirata, Shirley Ho, Bhuvnesh Jain, Christina D. Kreisch, Federico Marulli, Nelson Padilla, Giorgia Pollina, Martin Sahlén, Ravi K. Sheth, Rachel Somerville, Istvan Szapudi, Rien van de Weygaert, Francisco Villaescusa-Navarro, Benjamin D. Wandelt, and Yun Wang. Cosmic voids: a novel probe to shed light on our Universe. *Bulletin of the American Astronomical Society*, 51(3):40, May 2019. doi: 10.48550/arXiv.1903.05161.

[13] K. R. Mecke, T. Buchert, and H. Wagner. Robust morphological measures for large-scale structure in the Universe. *Astronomy and Astrophysics*, 288:697–704, August 1994. doi: 10.48550/arXiv.astro-ph/9312028.

[14] Siyao Cheng, Yuan-Sen Ting, Brice Ménard, and Joan Bruna. A new approach to observational cosmology using the scattering transform. *Monthly Notices of the Royal Astronomical Society*, 499(4):5902–5914, December 2020. doi: 10.1093/mnras/staa3165.

[15] Erwan Ally, T Marchand, J-F Cardoso, F Villaescusa-Navarro, S Ho, and S Mallat. New interpretable statistics for large-scale structure analysis and generation. *Physical Review D*, 102(10):103506, 2020.

[16] Janis Fluri, Tomasz Kacprzak, Alexandre Refregier, Adam Amara, Aurelien Lucchi, and Thomas Hofmann. Cosmological constraints from noisy convergence maps through deep learning. *Physical Review D*, 98(12):123518, 2018.

[17] Tom Charnock, Guilhem Lavaux, and Benjamin D. Wandelt. Automatic physical inference with information maximizing neural networks. *Physical Review D*, 97(8):083004, April 2018. doi: 10.1103/PhysRevD.97.083004.

[18] T. Lucas Makinen, Tom Charnock, Justin Alsing, and Benjamin D. Wandelt. Lossless, scalable implicit likelihood inference for cosmological fields. *Journal of Cosmology and Astroparticle Physics*, 2021(11):049, November 2021. doi: 10.1088/1475-7516/2021/11/049.

[19] Arushi Gupta, José Manuel Zorrilla Matilla, Daniel Hsu, and Zoltán Haiman. Non-Gaussian information from weak lensing data via deep learning. *Physical Review D*, 97(10):103515, May 2018. doi: 10.1103/PhysRevD.97.103515.

[20] Kyle Cranmer, Johann Brehmer, and Gilles Louppe. The frontier of simulation-based inference. *Proceedings of the National Academy of Sciences*, 117(48):30055–30062, 2020.

[21] Jens Jasche and Benjamin D. Wandelt. Bayesian physical reconstruction of initial conditions from large-scale structure surveys. *Monthly Notices of the Royal Astronomical Society*, 432(2):894–913, June 2013. doi: 10.1093/mnras/stt449.

[22] F. S. Kitaura. The initial conditions of the universe from constrained simulations. *Monthly Notices of the Royal Astronomical Society*, 429:L84–L88, February 2013. doi: 10.1093/mnrasl/sls029.

[23] Huiyuan Wang, H. J. Mo, Xiaohu Yang, Y. P. Jing, and W. P. Lin. ELUCID—Exploring the Local Universe with the Reconstructed Initial Density Field. I. Hamiltonian Markov Chain Monte Carlo Method with Particle Mesh Dynamics. *The Astrophysical Journal*, 794(1):94, October 2014. doi: 10.1088/0004-637X/794/1/94.

[24] Uroš Seljak, Grigor Aslanyan, Yu Feng, and Chirag Modi. Towards optimal extraction of cosmological information from nonlinear data. *Journal of Cosmology and Astroparticle Physics*, 2017(12):009, December 2017. doi: 10.1088/1475-7516/2017/12/009.

[25] Natalia Porqueres, Alan Heavens, Daniel Mortlock, and Guilhem Lavaux. Lifting weak lensing degeneracies with a field-based likelihood. *MNRAS*, 509(3):3194–3202, January 2022. doi: 10.1093/mnras/stab3234.

[26] Biwei Dai and Uroš Seljak. Translation and rotation equivariant normalizing flow (TRENF) for optimal cosmological analysis. *Monthly Notices of the Royal Astronomical Society*, 516(2):2363–2373, October 2022. doi: 10.1093/mnras/stac2010.

[27] Sultan Hassan, Francisco Villaescusa-Navarro, Benjamin Wandelt, David N. Spergel, Daniel Anglés-Alcázar, Shy Genel, Miles Cranmer, Greg L. Bryan, Romeel Davé, Rachel S. Somerville, Michael Eickenberg, Desika Narayanan, Shirley Ho, and Sambatra Andrianomena. HIFlow: Generating Diverse HI Maps Conditioned on Cosmology using Normalizing Flow. *arXiv e-prints*, art. arXiv:2110.02983, October 2021.

[28] Roy Friedman and Sultan Hassan. Higlow: Conditional normalizing flows for high-fidelity hi map modeling. *arXiv preprint arXiv:2211.12724*, 2022.

[29] Pascal J Elahi, Alexander Knebe, Frazer R Pearce, Chris Power, Gustavo Yepes, Weiguang Cui, Daniel Cunnuma, Scott T Kay, Federico Sembolini, Alexander M Beck, et al. nifty galaxy cluster simulations–iii. the similarity and diversity of galaxies and subhaloes. *Monthly Notices of the Royal Astronomical Society*, 458(1):1096–1116, 2016.

[30] Hung-Jin Huang, Tim Eifler, Rachel Mandelbaum, and Scott Dodelson. Modelling baryonic physics in future weak lensing surveys. *Monthly Notices of the Royal Astronomical Society*, 488(2):1652–1678, 2019.

[31] Francisco Villaescusa-Navarro, Daniel Anglés-Alcázar, Shy Genel, David N Spergel, Yin Li, Benjamin Wandelt, Andrina Nicola, Leander Thiele, Sultan Hassan, Jose Manuel Zorrilla Matilla, et al. Multifield cosmology with artificial intelligence. *arXiv preprint arXiv:2109.09747*, 2021.

[32] Annalisa Pillepich, Volker Springel, Dylan Nelson, Shy Genel, Jill Naiman, Rüdiger Pakmor, Lars Hernquist, Paul Torrey, Mark Vogelsberger, Rainer Weinberger, et al. Simulating galaxy formation with the *illustris* model. *Monthly Notices of the Royal Astronomical Society*, 473(3):4077–4106, 2018.

[33] Romeel Davé, Daniel Anglés-Alcázar, Desika Narayanan, Qi Li, Mika H Rafieferantsoa, and Sarah Appleby. Simba: Cosmological simulations with black hole growth and feedback. *Monthly Notices of the Royal Astronomical Society*, 486(2):2827–2849, 2019.

[34] E. Krause, T. F. Eifler, J. Zuntz, O. Friedrich, M. A. Troxel, S. Dodelson, J. Blazek, L. F. Secco, N. MacCrann, E. Baxter, C. Chang, N. Chen, M. Crocce, J. DeRose, A. Ferte, N. Kokron, F. Lacasa, V. Miranda, Y. Omori, A. Porredon, R. Rosenfeld, S. Samuroff, M. Wang, R. H. Wechsler, T. M. C. Abbott, F. B. Abdalla, S. Allam, J. Annis, K. Bechtol, A. Benoit-Levy, G. M. Bernstein, D. Brooks, D. L. Burke, D. Capozzi, M. Carrasco Kind, J. Carretero, C. B. D’Andrea, L. N. da Costa, C. Davis, D. L. DePoy, S. Desai, H. T. Diehl, J. P. Dietrich, A. E. Evrard, B. Flaugher, P. Fosalba, J. Frieman, J. Garcia-Bellido, E. Gaztanaga, T. Giannantonio, D. Gruen, R. A. Gruendl, J. Gschwend, G. Gutierrez, K. Honscheid, D. J. James, T. Jeltema, K. Kuehn, S. Kuhlmann, O. Lahav, M. Lima, M. A. G. Maia, M. March, J. L. Marshall, P. Martini, F. Menanteau, R. Miquel, R. C. Nichol, A. A. Plazas, A. K. Romer, E. S. Rykoff, E. Sanchez, V. Scarpine, R. Schindler, M. Schubnell, I. Sevilla-Noarbe, M. Smith, M. Soares-Santos, F. Sobreira, E. Suchyta, M. E. C. Swanson, G. Tarle, D. L. Tucker, V. Vikram, A. R. Walker, and J. Weller. Dark Energy Survey Year 1 Results: Multi-Probe Methodology and Simulated Likelihood Analyses. *arXiv e-prints*, art. arXiv:1706.09359, June 2017.

[35] Peter L Taylor, Francis Bernardeau, and Thomas D Kitching. k-cut cosmic shear: Tunable power spectrum sensitivity to test gravity. *Physical Review D*, 98(8):083514, 2018.

[36] E. Krause, X. Fang, S. Pandey, L. F. Secco, O. Alves, H. Huang, J. Blazek, J. Prat, J. Zuntz, T. F. Eifler, N. MacCrann, J. DeRose, M. Crocce, A. Porredon, B. Jain, M. A. Troxel, S. Dodelson, D. Huterer, A. R. Liddle, C. D. Leonard, A. Amon, A. Chen, J. Elvin-Poole, A. Ferté, J. Muir, Y. Park, S. Samuroff, A. Brandao-Souza, N. Weaverdyck, G. Zacharek, R. Rosenfeld, A. Campos, P. Chintalapati, A. Choi, E. Di Valentino, C. Doux, K. Herner, P. Lemos, J. Mena-Fernández, Y. Omori, M. Paterno, M. Rodriguez-Monroy, P. Rogozenski, R. P. Rollins, A. Troja, I. Tutasaus, R. H. Wechsler, T. M. C. Abbott, M. Aguena, S. Allam, F. Andrade-Oliveira, J. Annis, D. Bacon, E. Baxter, K. Bechtol, G. M. Bernstein, D. Brooks, E. Buckley-Geer, D. L. Burke, A. Carnero Rosell, M. Carrasco Kind, J. Carretero, F. J. Castander, R. Cawthon, C. Chang, M. Costanzi, L. N. da Costa, M. E. S. Pereira, J. De Vicente, S. Desai, H. T. Diehl, P. Doel, S. Everett, A. E. Evrard, I. Ferrero, B. Flaugher, P. Fosalba, J. Frieman, J. García-Bellido, E. Gaztanaga, D. W. Gerdes, T. Giannantonio, D. Gruen, R. A. Gruendl, J. Gschwend, G. Gutierrez, W. G. Hartley, S. R. Hinton, D. L. Hollowood, K. Honscheid, B. Hoyle, E. M. Huff, D. J. James, K. Kuehn, N. Kuropatkin, O. Lahav, M. Lima, M. A. G. Maia, J. L. Marshall, P. Martini, P. Melchior, F. Menanteau, R. Miquel, J. J. Mohr, R. Morgan, J. Myles, A. Palmese, F. Paz-Chinchón, D. Petravick, A. Pieres, A. A. Plazas Malagón, E. Sanchez, V. Scarpine, M. Schubnell, S. Serrano, I. Sevilla-Noarbe, M. Smith, M. Soares-Santos, E. Suchyta, G. Tarle, D. Thomas, C. To, T. N. Varga, and J. Weller. Dark Energy Survey Year 3 Results: Multi-Probe Modeling Strategy and Validation. *arXiv e-prints*, art. arXiv:2105.13548, May 2021.

[37] Cyrille Doux, E. Baxter, Pablo Lemos, C. Chang, A. Alarcon, A. Amon, A. Campos, A. Choi, M. Gatti, D. Gruen, et al. Dark energy survey internal consistency tests of the joint cosmological probes analysis with posterior predictive distributions. *Monthly Notices of the Royal Astronomical Society*, 503(2):2688–2705, 2021.

[38] Stephane G Mallat. A theory for multiresolution signal decomposition: the wavelet representation. *IEEE transactions on pattern analysis and machine intelligence*, 11(7):674–693, 1989.

[39] J-L Starck and Fionn Murtagh. *Astronomical image and data analysis*. Springer Science & Business Media, 2007.

[40] Alfred Haar. Zur theorie der orthogonalen funktionensysteme. *Mathematische Annalen.*, 69(3):331–371, 1910. ISSN 0025-5831.

[41] Ingrid Daubechies. Orthonormal bases of compactly supported wavelets. *Communications on pure and applied mathematics*, 41(7):909–996, 1988.

[42] Laurent Dinh, Jascha Sohl-Dickstein, and Samy Bengio. Density estimation using real NVP. In *5th International Conference on Learning Representations, ICLR*

2017, Toulon, France, April 24-26, 2017, Conference Track Proceedings. OpenReview.net, 2017. URL <https://openreview.net/forum?id=HkpbnH91x>.

[43] George Papamakarios, Iain Murray, and Theo Pavlakou. Masked autoregressive flow for density estimation. In Isabelle Guyon, Ulrike von Luxburg, Samy Bengio, Hanna M. Wallach, Rob Fergus, S. V. N. Vishwanathan, and Roman Garnett, editors, *Advances in Neural Information Processing Systems 30: Annual Conference on Neural Information Processing Systems 2017, December 4-9, 2017, Long Beach, CA, USA*, pages 2338–2347, 2017.

[44] Diederik P. Kingma and Prafulla Dhariwal. Glow: Generative flow with invertible 1x1 convolutions. In Samy Bengio, Hanna M. Wallach, Hugo Larochelle, Kristen Grauman, Nicolò Cesa-Bianchi, and Roman Garnett, editors, *Advances in Neural Information Processing Systems 31: Annual Conference on Neural Information Processing Systems 2018, NeurIPS 2018, December 3-8, 2018, Montréal, Canada*, pages 10236–10245, 2018.

[45] Jason J Yu, Konstantinos G Derpanis, and Marcus A Brubaker. Wavelet flow: Fast training of high resolution normalizing flows. *Advances in Neural Information Processing Systems*, 33:6184–6196, 2020.

[46] Sergey Ioffe and Christian Szegedy. Batch normalization: Accelerating deep network training by reducing internal covariate shift. In *International conference on machine learning*, pages 448–456. PMLR, 2015.

[47] Joeri Hermans, Arnaud Delaunoy, François Rozet, Antoine Wehenkel, and Gilles Louppe. Averting A crisis in simulation-based inference. *CoRR*, abs/2110.06581, 2021. URL <https://arxiv.org/abs/2110.06581>.

[48] Simon Duane, Anthony D Kennedy, Brian J Pendleton, and Duncan Roweth. Hybrid monte carlo. *Physics letters B*, 195(2):216–222, 1987.

[49] Core Francisco Park, Erwan Ally, Francisco Villaescusa-Navarro, and Douglas P Finkbeiner. Quantification of high dimensional non-gaussianities and its implication to fisher analysis in cosmology. *arXiv preprint arXiv:2204.05435*, 2022.

[50] Dezső Ribli, Bálint Ármin Pataki, José Manuel Zorrilla Matilla, Daniel Hsu, Zoltán Haiman, and István Csabai. Weak lensing cosmology with convolutional neural networks on noisy data. *Monthly Notices of the Royal Astronomical Society*, 490(2):1843–1860, December 2019. doi: 10.1093/mnras/stz2610.

[51] Tianhuan Lu, Zoltán Haiman, and José Manuel Zorrilla Matilla. Simultaneously constraining cosmology and baryonic physics via deep learning from weak lensing. *Monthly Notices of the Royal Astronomical Society*, 511(1):1518–1528, March 2022. doi: 10.1093/mnras/stac161.

[52] Giovanni Aricò, Raul E. Angulo, Carlos Hernández-Monteagudo, Sergio Contreras, Matteo Zennaro, Marcos Pellejero-Ibañez, and Yetli Rosas-Guevara. Modelling the large-scale mass density field of the universe as a function of cosmology and baryonic physics. *Monthly Notices of the Royal Astronomical Society*, 495(4):4800–4819, July 2020. doi: 10.1093/mnras/staa1478.

[53] Hiroaki Aihara, Nobuo Arimoto, Robert Armstrong, Stéphane Arnouts, Neta A Bahcall, Steven Bickerton, James Bosch, Kevin Bundy, Peter L Capak, James HH Chan, et al. The hyper suprime-cam ssp survey: overview and survey design. *Publications of the Astronomical Society of Japan*, 70(SP1):S4, 2018.

[54] Rene Laureijs, J Amiaux, S Arduini, J-L Auguera, J Brinchmann, R Cole, M Cropper, C Dabin, L Duvet, A Ealet, et al. Euclid definition study report. *arXiv preprint arXiv:1110.3193*, 2011.

[55] Željko Ivezić, Steven M Kahn, J Anthony Tyson, Bob Abel, Emily Acosta, Robyn Allsman, David Alonso, Yusra AlSayyad, Scott F Anderson, John Andrew, et al. Lsst: from science drivers to reference design and anticipated data products. *The Astrophysical Journal*, 873(2):111, 2019.

[56] Volker Springel. The cosmological simulation code GADGET-2. *Monthly Notices of the Royal Astronomical Society*, 364(4):1105–1134, December 2005. doi: 10.1111/j.1365-2966.2005.09655.x.

[57] Peter Schneider, Jürgen Ehlers, and Emilio E. Falco. *Gravitational Lenses*. 1992. doi: 10.1007/978-3-662-03758-4.

[58] Tianhuan Lu and Zoltán Haiman. The impact of baryons on cosmological inference from weak lensing statistics. *Monthly Notices of the Royal Astronomical Society*, 506(3):3406–3417, September 2021. doi: 10.1093/mnras/stab1978.

[59] A. Petri. Mocking the weak lensing universe: The LensTools Python computing package. *Astronomy and Computing*, 17:73–79, October 2016. doi: 10.1016/j.ascom.2016.06.001.

[60] Stéphane Mallat. Group invariant scattering. *Communications on Pure and Applied Mathematics*, 65(10):1331–1398, 2012.

[61] Sihao Cheng and Brice Ménard. Weak lensing scattering transform: dark energy and neutrino mass sensitivity. *Monthly Notices of the Royal Astronomical Society*, 507(1):1012–1020, 2021.

[62] Georgios Valogiannis and Cora Dvorkin. Towards an optimal estimation of cosmological parameters with the wavelet scattering transform. *Physical Review D*, 105(10):103534, 2022.

[63] Tianhuan Lu, Zoltán Haiman, and Xiangchong Li. Cosmological constraints from hsc survey first-year data using deep learning. *arXiv preprint arXiv:2301.01354*, 2023.